

# 3-D Crustal Shear Wave Velocity Model Derived from the Adjoint Waveform Tomography in the Central Japan Island

Kota Mukumoto<sup>1</sup>, Takeshi Tsuji<sup>1,2,3</sup>

<sup>1</sup> Department of Earth Resources Engineering, Kyushu University, Fukuoka, Japan

<sup>2</sup> Faculty of Engineering, The University of Tokyo, Tokyo, Japan

<sup>3</sup> International Institute for Carbon-Neutral Energy Research (I2CNER), Kyushu University, Fukuoka, Japan

8 June 2022

## SUMMARY

Adjoint waveform tomography, which is an emerging seismic imaging method for the crust- and global-scale problems, has gained popularity in the past and present decade. This study, for first time, applies adjoint waveform tomography to the large volume of seismic data recorded by the densely spaced, permanent monitoring network that covers the entirety of Japan. We develop a heterogeneous shear-wave velocity model of central Japan that agrees with the geology and lithology. The results reduce the time-frequency phase misfit by 16.4% in the 0.02–0.05 Hz frequency band and 6.7% in the 0.033–0.1 Hz band, respectively. We infer that some velocity anomalies resolved in this work would reflect the subsurface structures such as the volcanic fluids, dehydration of the subducted crust, and sedimentary basin. In addition, dense distributions of deep earthquakes are visible beneath the high-velocity blocks estimated in this study. The results of this study suggest the possibility of imaging large scale heterogeneous subsurface structures using waveform tomography with a densely distributed network of permanent seismometers.

Key words: Crustal structure, Crustal imaging, Waveform inversion, Seismic tomography in Japan

## 1 1 INTRODUCTION

2 The island nation of Japan is located on the convergent boundary where the Philippine Sea  
3 plate and the Pacific plate are subducting beneath the Eurasian and the Okhotsk plates.  
4 The interactions of these four main plates are responsible for many of Japan's unique tec-  
5 tonic features (Figure 1). The boundary between the Pacific and Eurasian plates on land is  
6 the Itoigawa– Shizuoka tectonic line (ISTL), which extends from Itoigawa city in Niigata  
7 prefecture to Shizuoka city in Shizuoka prefecture. The subduction of the Philippine Sea  
8 Plate created the Izu–Bonin (arc–arc) collision zone (IBCZ), where the Izu–Bonin arc has  
9 collided with the Honshu arc. The area also includes two prominent structural features: the  
10 Median tectonic line (MTL) and the Niigata–Kobe tectonic line (NKTL). Central Japan  
11 contains many active volcanoes, sedimentary basins, the IBCZ, and several major tectonic  
12 lines (ISTL, MTL, and NKTL). Therefore, the seismic structure of the region is expected  
13 to contain substantial lateral heterogeneities. The complex geological structures of central  
14 Japan have been the subject of many previous geophysical studies, which have relied mainly  
15 on regional- and exploration-scale seismic tomography (Arai et al., 2013; Arai & Iwasaki,  
16 2014; Nakajima & Hasegawa, 2007a, 2007b; Nakajima et al., 2009; Hirose et al., 2008; Nishida  
17 et al., 2008; Nimiya et al., 2020; Miyoshi et al., 2017). For example, a series of studies us-  
18 ing first-arrival tomography (Nakajima & Hasegawa, 2007a, 2007b; Nakajima et al., 2009)  
19 revealed the slab geometry of the Philippine Sea Plate and investigated plausible relation-  
20 ships between the arc magmatism and the subducting oceanic plates. Nishida et al. (2008)  
21 and Nimiya et al. (2020) leveraged the ambient noise wavefield using seismic interference  
22 and clearly imaged underground structures including magmatic fluids and thick sedimentary  
23 successions. Recently, the development of adjoint waveform tomography techniques has im-  
24 proved our ability to resolve subsurface structures (Fichtner et al., 2009, 2010; Tape et al.,  
25 2010; Simute et al., 2016; Lei et al., 2020). In this method, three-dimensional (3D) sensitivity  
26 distributions of seismic waves can be computed by full numerical seismic wave simulation in  
27 heterogeneous media using the adjoint method (Tarantola, 1984; Mora, 1987; Tromp et al.,  
28 2005; Fichtner, 2010). Furthermore, first-arrival tomography and ambient noise tomography

29 use specific seismic phases, whereas adjoint waveform tomography can use as much waveform  
30 information as possible without requiring selections of seismic phases. Miyoshi et al. (2017)  
31 firstly applied adjoint tomography using broad band seismic stations of F-net in Kanto area  
32 and obtained stronger heterogeneous velocity model compared to the one estimated using  
33 ray-tomography. Therefore, the application of adjoint waveform tomography might improve  
34 tomographic imaging of heterogeneous seismic velocity structures beneath central Japan.

35 The goals of the present work are to resolve crustal S-wave velocity structures in central  
36 Japan based on adjoint waveform tomography, and to investigate whether it is possible to  
37 obtain detailed tomographic images comparable to those resolved by other popular methods  
38 (e.g., first-arrival or ambient noise tomography). Here, we apply adjoint waveform tomogra-  
39 phy to the large volume of seismic data collected by Hi-net and F-net (Okada et al., 2004).  
40 The estimated crustal S-wave velocity model reaches a minimum misfit after 17 iterations  
41 and shows strong lateral velocity variations. The velocity anomalies in the estimated model  
42 are in good agreement with the geology.

## 43 2 METHOD

### 44 2.1 3D seismic wave simulation and initial model

Synthetic waveforms of 240 sec were calculated using the spectral element method, which is widely used in seismology due to its accuracy and ease of code parallelisation (Komatitsch & Tromp, 1999, 2002). We used the program SPECFEM3D Cartesian for forward and adjoint 3D isotropic seismic wave simulations (Peter et al., 2011). We calculated seismic wavefields in our target model volume of  $133.5^{\circ}$ – $140.5^{\circ}$  in longitude  $\times$   $32.5^{\circ}$ – $37.5^{\circ}$  in latitude  $\times$  0–90 km in depth with mesh accurate up to seismic wave of 2.5 sec period. The laterally homogeneous seismic velocity model named JMA2001 was used as the initial model (Ueno et al., 2002); this provides S- and P- wave velocity structures around Japan. We obtained initial density structures using empirical relationship between P-wave velocity and density

(Brocher, 2005):

$$\rho = 1.6612V_p - 0.4721V_p^2 + 0.0671V_p^3 - 0.0043V_p^4 + 0.000106V_p^5, \quad (1)$$

where  $\rho$  is in  $g/cm^3$  and  $V_p$  is in  $km/sec$ .

## 2.2 Computation of misfit function

Noisy observed data, which is dissimilar to synthetic data, could result in incorrect model parameters. In addition, cycle skipping can lead to a local minimum in the waveform inversion's solution space that does not correspond to true structure. The latter phenomenon can occur when observed waveforms are more than half a wavelength out of phase from synthetic waveforms; therefore, data selection must be carried out as carefully as possible to prevent this. In this study, we automatically determine the time-windows of pairs of synthetic and observed waveforms based on parameters such as time lag, the cross-correlation coefficient between observed and synthetic waveforms, and the signal-to-noise ratio, using the program FLEXWIN (Maggi et al., 2009). We optimized the model parameters in two frequency ranges: 0.02–0.05 and 0.0333–0.1 Hz, and time-window selection was carried out before the first iteration for each frequency range. We set the maximum time lag between observed and synthetic waveforms to 12 *sec* during selections of time-windows for 0.02–0.05 *Hz* and 5 *sec* for 0.033–0.1 *Hz*. As a result, time-windows were determined for 2,860 waveform pairs in 0.02–0.5 Hz and 15,523 in 0.033–0.1 Hz. The quantification of the misfit between synthetic and observed data was based on phase misfit using the time-frequency transform (Fichtner et al., 2008, 2009):

$$E_p^2(u_i^0, u_i) = \iint W_p^2(t, \omega) W_t(t)^2 [\phi_i(t, \omega) - \phi_i^0(t, \omega)]^2 dt d\omega, \quad (2)$$

where  $u_i^0$  and  $u_i$  are  $i$ th component observed and synthetic velocity data,  $\phi_i^0$  and  $\phi_i$  are time-frequency phase of observed and synthetic velocity data,  $W_t$  is time window selected by FLEXWIN and  $W_p$  is weighting function. The weighting function in this study was chosen

3-D Crustal Shear Wave Velocity Model Derived from the Adjoint Waveform Tomography in the Central  
 by following Fichtner et al (2008):

$$W_p = \log(1 + |\tilde{u}|) / \max_{t,\omega} \log(1 + |\tilde{u}|), \quad (3)$$

where  $\tilde{u}$  is the velocity data on the time-frequency plane.

### 2.3 Model update

We used a multiscale strategy that first recovers the smooth structures, then resolve finer-scale structures by broadening the frequency range (from 0.02–0.05 to 0.033–0.1 Hz). The most energetic phase in our data is the surface wave; therefore, only the S-wave velocity was updated between iterations.

We computed gradient of misfit function with respect to model parameter using the adjoint method, then updated model in the scheme of Newton’s method. Approximate inverse hessian kernels were applied to gradients of each event. This inverse hessian kernel acts as a preconditioner in Newton’s method (Tape et al., 2010). Model update at  $i + 1$ th iteration in this study is

$$m_{i+1} = m_i - \alpha S[\tilde{H}^{-1}(m_i)g(m_i)], \quad (4)$$

where  $m_i$  is current model parameter,  $\alpha$  is step length which scales descent direction,  $\tilde{H}(m)$  is approximate hessian,  $g(m)$  is gradient of misfit function, and  $S$  is smoothing operator. Smoothing of the gradient was performed by convolution with a 3D Gaussian. Based on the bandwidth of the data and inspired by Chow et al. (2022), we set horizontal and vertical standard deviations of the 3D Gaussian to 20 and 10 *km* for 0.02–0.05 *Hz*, and 10 and 6 *km* for 0.033–0.1 *Hz*. Step length  $\alpha_{x\%}$  was determined using following manner at each iteration to select enough small step length ( $\alpha_{x\%}$  means that step length is set so that the change between current model  $m_i$  and updated model  $m_{i+1}$  is  $< x\%$ ).

(i) Two total misfits using  $\alpha_{x\%}$  and  $\alpha_{x+1\%}$  were calculated before going to next iteration and adopted  $\alpha_{x\%}$  if misfit of  $\alpha_{x\%}$  is  $> \alpha_{x+1\%}$ .

(ii) Step length  $\alpha_{x\%}$  is reduced to  $\alpha_{x/2\%}$  if misfit of  $\alpha_{x\%}$  is  $< \alpha_{x+1\%}$ .

(iii) Step length is increased to  $\alpha_{2 \times x\%}$  from  $\alpha_{x\%}$  only if reductions of misfits compared to previous iteration are  $< 1\%$  over past 2 iterations.

We firstly employed  $\alpha_{2\%}$  and changed step length at each iteration by following above manner. When misfit of updated model  $m_{i+1}$  is larger than one of current model  $m_i$ , we stopped inversion at  $i$ th iteration.

### 3 DATA

Earthquake waveform data were collected from the Hi-net high-sensitivity seismograph network and F-net broad-band seismograph network, operated across Japan by the National Research Institute for Earth Science and Disaster Prevention (NIED) (Okada et al., 2004). There are 388 Hi-net and 28 F-net permanent stations in our study area (Figure 2(a)), all have three-component velocity seismometers and are deployed in boreholes. We used F-net stations for the inversion of 0.02–0.05 and 0.033–0.1  $Hz$ , while Hi-net stations were used only for 0.033–0.1  $Hz$ . The seismometers of Hi-net are designed to have sensitivities  $>1.0$  Hz; however, our target frequency range is 0.02–0.1 Hz. Therefore, we applied the sensitivity corrections proposed by Maeda et al. (2011) to enhance low-frequency component and used Hi-net data in the inversion only for higher frequency range 0.033–0.1  $Hz$ .

We collected data from 41 earthquakes that occurred between 2004 and 2021 with moment magnitudes  $4.4 \leq Mw \leq 5.5$  and depths shallower than 60 km (Figures 2). We prepared inversion dataset and validation dataset. Inversion dataset includes 29 earthquakes data and was used for the inversion of S-wave velocity model, while validation dataset consisting 12 earthquakes was used for only the validation of resultant model. Earthquakes in the validation dataset were chosen so that their locations do not overlap with those in the inversion dataset (Figures 2(b) and 2(c)). Earthquake parameters for simulations were extracted from their Global CMT solutions (Ekström et al., 2012); these values were fixed while updating our velocity models, because inversion for source parameter updates requires additional computation time. In addition, we restricted the data to recordings at source–receiver distances of  $>80$  km.

## 91 4 RESULTS AND INTERPRETATIONS

92 After 11 iterations of the 0.02–0.05 Hz band and 6 iterations of the 0.033–0.1 Hz band we  
 93 obtained the S-wave velocity model shown in Figures 3. The S-wave velocity outside the  
 94 dashed lines in Figures 3 cannot be accurately estimated due to the less sensitivity of our  
 95 inversion dataset (discussed later). The results show strong horizontal velocity variations:  
 96 for example, at 5 km depth, low-velocity anomalies reach  $<3000$  m/s, whereas high-velocity  
 97 anomalies are  $\sim 4000$  m/s. The misfit is reduced by 16.4% in the 0.02–0.05 Hz band and  
 98 6.7% in the 0.033–0.1 Hz band (Figure 4).

99 We confirmed that the misfits between observed and synthetic waveforms were improved  
 100 after 17 iterations; representative examples are shown in figures 5. Not only phases but  
 101 also amplitudes are improved after 17 iterations. However, unchanged waveforms between  
 102 after and before inversion can be seen in horizontal components of panel D. This can be  
 103 happened due to inappropriate earthquake source parameter or insufficient model param-  
 104 eterization (elastic isotropic parameterization in our study). Therefore, there is chance to  
 105 improve our velocity model by including inversions of earthquake source parameters and  
 106 elastic anisotropic parameters. This is a part of our future study.

107 The largest feature in the resultant S-wave velocity model at shallower depths  $\leq 10$  km is  
 108 that the northern part of the study area where active volcanoes exist is characterized by low  
 109 velocities, whereas high velocities dominate in the south. This general finding agrees with  
 110 previous studies (J. Nakajima & Hasegawa, 2007a; Nishida et al., 2008). At shallow depths,  
 111 there is a distinct low-velocity anomaly around region A. The Niigata sedimentary basin,  
 112 which formed during the opening of the Japan Sea (Takano, 2002), covers a portion of this  
 113 low-velocity anomaly. In addition, multiple active volcanoes, such as Asama mountain and  
 114 Kusatsu–Shirane mountain, are in this region. Therefore, the low-velocity anomaly could be  
 115 due in part to the sedimentary basin as well as magmatic fluids associated with back-arc  
 116 volcanism. The high-velocity anomalies aligned from southwest to northeast were imaged at  
 117 depths  $\leq 10$  km (B1–B3 in figures 3). These anomalies partially agree with previous model  
 118 derived from ambient noise tomography (Nishida et al., 2008). Figures 6(a) and (b) show

119 the S-wave velocity at 10 *km* with epicenters of shallow earthquakes (0–25 *km*) and deep  
 120 earthquakes (25–50 *km*). The hypocenters of earthquakes shown in Figures 6(a) and (b) was  
 121 taken from JUICE catalog (Yano et al., 2017). Correlation between high-velocity anomalies  
 122 and shallow earthquakes are unclear, while there is dense distributions of deep earthquakes  
 123 around high-velocity blocks B1–B3.

124 At deeper depths  $\leq 25$  *km*, four low-velocity anomalies appear in the south; regions C1,  
 125 C2, D, and E. The boundary between the Philippine Sea Plate and the Eurasian Plate around  
 126 C1, C2 and D is around 30 *km* depth (Hirose et al., 2008; J. Nakajima et al., 2009), thus,  
 127 the dehydrated fluid from the hydrous minerals of the subducted oceanic crust would be one  
 128 of the interpretations of lower seismic velocity. The region around IBCZ (between C1 and  
 129 C2) is characterized by no lower S-wave velocity. Seno and Yamasaki (2003) hypothesized  
 130 that there is no or less dehydration reactions in the subducted slab beneath the IBCZ. In  
 131 addition, Arai et al. (2013) imaged the subsurface structure at IBCZ using active-seismic  
 132 data and proposed that thick crust of Izu-Bonin arc above the oceanic crust result in less  
 133 infiltration of seawater to oceanic crust. Based on these studies, we infer that absence of low  
 134 velocity anomaly around IBCZ is caused by less dehydration due to the existence of thick  
 135 crust of Izu-Bonin arc. Lower seismic velocities of region D is located beneath the chain of  
 136 active volcanoes of Izu-Bonin arc and might be related with magmatic activities of active  
 137 volcanoes.

138 Figure 6(c) shows the S-wave velocity at 25 *km* depth with distributions of low-frequency  
 139 earthquakes (LFEs) estimated by Kato et al. (2020). Nakajima and Hasegawa. (2016) re-  
 140 vealed that P-wave velocity above the subducted plate is low above places where activities  
 141 of LFEs are less, however velocity is normal above places where there is activities of LFEs  
 142 (Ise gaps and Tokai region in Figure 6 (c)). Therefore, the existence of lower S-wave velocity  
 143 at region D, C1, and C2 is well consistent with observations of their study.

## 144 5 DISCUSSION

We conducted resolution analysis using point spread functions (PSFs) to assess the tomographic inversions of this study. PSFs are point-localized perturbations from background models. Estimating the response of a tomographic inversion to PSFs allows to evaluate how much blur and smear are generated (Fichtner and Trampert, 2011). In this study, we computed Hessian on a model perturbation using approximated equation

$$H(m)\delta m \approx g(m + \delta m), \quad (5)$$

145 where  $H(m)$  denotes the Hessian at the final model  $m$ ,  $\delta m$  is perturbations and  $g(m + \delta m)$   
 146 is the gradient of perturbed model. We computed responses  $H\delta m$  for lower frequency  
 147 range 0.02–0.05  $Hz$  only and applied smoothing using 3D Gaussian with same deviations in  
 148 our velocity inversion. Figures 7 show the results of individual PSFs tests for some interest  
 149 velocity anomalies B1–B3, C1, C2, and D in our velocity model. We put 3D Gaussian  
 150 functions with horizontal and vertical standard deviations of 15 and 6  $km$  as a  $\delta m$ . Localized  
 151  $\delta m$  is located at 7  $km$  depth and has -15% peak perturbation for high-velocity anomalies  
 152 B1–B3, while  $\delta m$  is located at 25  $km$  depth with +15% peak perturbations for low-velocity  
 153 anomalies C1, C2, and D. The results of PSFs tests for B2 and B3 (Figures 7(b) and (c)) show  
 154 that peaks of  $H\delta m$  are well coincide with the locations of velocity perturbations and support  
 155 the existence of high-velocity anomalies at B2 and B3. However, large vertical smearing can  
 156 be seen in the result of PSF test for B1 (Figure 7(a)). This suggests that actual termination  
 157 of high-velocity zone of B1 extending to 35  $km$  depth seems to be shallower than our velocity  
 158 model. Velocity perturbations are accurately mapped to  $H\delta m$  in the results of PSFs tests  
 159 for C1, C2 and D although the peaks are slightly shifted (Figures 7(d), (e) and (f)). There  
 160 is no large smearing like result for B1 and we conclude that detected low-velocity anomalies  
 161 C1, C2 and D accurately reflect the existence of dehydrated fluids around 25  $km$  depth.

162 To investigate how much our configurations of inversion such as limited frequency bands  
 163 and source-station pairs have a sensitivity to target model volume, we computed  $H\delta m$  by  
 164 replacing  $\delta m$  of PSFs test with 50  $m/s$  of constant volumetric velocity perturbation. The

165 Hessian respected to volumetric constant velocity perturbation corresponds to the zero-  
 166 wavenumber component of Hessian in frequency-wavenumber domain (Fichtner and Tram-  
 167 pert, 2011). Figures 8 show the normalized response to the constant volumetric velocity  
 168 perturbation at each frequency band. As expected,  $H\delta m$  of lower frequency band has large  
 169 values at greater depth compared to the one of higher frequency band. The largest values  
 170 of  $H\delta m$  are shallower than 40 km depth and no or very low sensitivity at depth  $\leq 60$  km.  
 171 Therefore, 90 km depth of our model volume is enough deep to compute seismic waves in-  
 172 cluded in our data set. We set 0.2 of threshold value to exclude regions where sensitivity is  
 173 not enough high from our interpretations of velocity models (dashed lines in Figures 3, 6,  
 174 and 8).

Validation dataset (Figure 2(c)) which was not included in inversion offer additional  
 information about results of inversion. If there is no or less misfit reduction of validation  
 data set, solutions of inversion could be overestimated. To estimate not only time-frequency  
 phase misfit but also other measurements, we employs normalized waveform difference misfit

$$E^2(m) = \frac{\int [u^{obs}(t) - u(t, m)]^2 dt}{\sqrt{\int u^{obs}(t)^2 dt \int u(t, m)^2 dt}} \quad (6)$$

175 used in previous studies, for example, Tape et al. (2010) and Simute et al. (2016).  $u^{obs}(t)$   
 176 and  $u(t, m)$  in equation (6) are observed and synthetic data. We used validation dataset  
 177 in frequency range 0.033–0.1 Hz, not in entire frequency range 0.02–0.1 Hz to include Hi-  
 178 net data in validation dataset. The validation dataset was selected by FLEXWIN as well  
 179 as the inversion dataset, however, we didn't employ any time-windows for the measure of  
 180 normalized waveform difference misfit. Figure 9 shows the histograms of normalized wave-  
 181 form difference of initial and final model for validation dataset. Improvement of misfit in  
 182 validation dataset suggests our inversion estimated meaningful velocity structures.

## 183 6 CONCLUSIONS

184 From seismic waveforms of 29 earthquakes recorded by 388 Hi-net and 28 F-net seismic  
 185 stations we built a 3D S-wave velocity model using adjoint waveform tomography. The model

186 estimation procedure was designed to minimize the time-frequency phase misfit between  
187 observed and synthetic seismic waveforms in the frequency bands 0.02–0.05 and 0.033–0.1  
188 Hz. The final model resolves strong horizontal heterogeneities, with velocity values in the  
189 range 2800–4000 m/s. The low-velocity anomalies resolved in the present work appear to  
190 correspond to a thick sedimentary basin, volcanic fluids, and fluids related to dehydration  
191 of subducted plate. We imaged clearly three high velocity blocks at shallow depths  $\leq 10$   
192 km, and there is intense seismicity beneath these high velocity blocks. Based on PSFs test,  
193 our dataset has enough sensitivity at regions of detected low- and high-velocity anomalies.  
194 In addition, the improved fit between observed and calculated waveforms obtained with our  
195 final model and evaluation using additional dataset which was not included in inversion  
196 support the accuracy of the results. This study confirms that adjoint waveform tomography  
197 and mixed dataset of F-net stations and densely distributed Hi-net stations in Japan can  
198 resolve S-wave velocity structure and explain known geology, yielding results comparable to  
199 other velocity models and seismic waveforms similar to observed data. Although we have not  
200 yet confirmed that earthquake data recorded by F-net and Hi-net stations have sufficient  
201 resolution for other regions characterized by complex geologic features, such as Kyushu and  
202 Hokkaido, the combination of adjoint waveform tomography, F-net and Hi-net station data  
203 will lead to accurate velocity models throughout the Japanese islands.

## 204 7 ACKNOWLEDGMENTS

205 This work was supported by the Japan Society for the Promotion of Science (JSPS) through  
206 a Grant-in-Aid for JSPS Research Fellow (JP21J21871). We used the open-source soft-  
207 ware SPECFEM3D Cartesian for seismic wave simulation and we thank the developers  
208 of SPECFEM3D. We also thank the National Research Institute for Earth Science and  
209 Disaster Prevention (NIED) for providing us with Hi-net data. Seismic wave simulations  
210 were conducted on the ITO supercomputer system at the Research Institute for Information  
211 Technology, Kyushu University. We used the open-source software GMT (Generic Mapping  
212 Tools)(Wessel et al., 2013) to construct figures.

## 213 8 DATA AVAILABILITY

214 The Hi-net data is available from <https://hinetwww11.bosai.go.jp/auth/?LANG=en>. The  
215 CMT solutions used in this study are available from <https://www.globalcmt.org/>. The S-  
216 wave velocity model we built is available at <https://doi.org/10.6084/m9.figshare.20024279>.

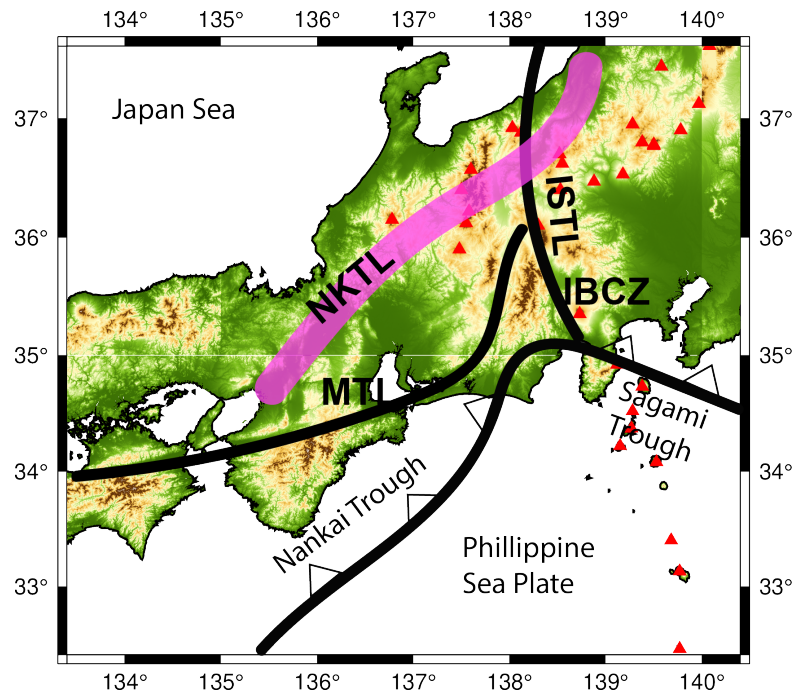
## 217 REFERENCES

- 218 Arai, R., Iwasaki, T., Sato, H., Abe, S., & Hirata, N., 2013. Crustal structure of the Izu collision  
219 zone in central Japan from seismic refraction data. *Journal of Geophysical Research: Solid Earth*  
220 118(12), 6258–6268.
- 221 Arai, R., & Iwasaki, T., 2014. Crustal structure in the northwestern part of the Izu collision zone  
222 in central Japan. *Earth, Planets and Space* 66(1), 1–12.
- 223 Brocher, T. M., 2005. Empirical relations between elastic wave speeds and density in the earth's  
224 crust. *Bulletin of the Seismological Society of America* 95(6), 2081–2092.
- 225 Chow, B., Kaneko, Y., Tape, C., Modrak, R., Mortimer, N., Bannister, Stephen., & Townend,  
226 J., 2022. Strong Upper-Plate Heterogeneity at the Hikurangi Subduction Margin (North Island,  
227 New Zealand) Imaged by Adjoint Tomography. *Journal of Geophysical Research: Solid Earth*  
228 127, e2021JB022865.
- 229 Ekström, G., Nettles, M., & Dziewoński, A. M., 2012. The global CMT project 2004–2010: Centroid-  
230 moment tensors for 13,017 earthquakes. *Physics of the Earth and Planetary Interiors* 200, 1–9.
- 231 Fichtner, A., Kennett, B. L. N., Igel, H., & Bunge, H. P., 2008. Theoretical background for  
232 continental- and global-scale full-waveform inversion in the time–frequency domain. *Geophysical*  
233 *Journal International* 175(2), 665–685.
- 234 Fichtner, A., Kennett, B. L. N., Igel, H., & Bunge, H. P., 2009. Full seismic waveform tomography  
235 for upper-mantle structure in the Australasian region using adjoint methods. *Geophysical Journal*  
236 *International* 179(3), 1703–1725.
- 237 Fichtner, A., 2010. *Full seismic waveform modelling and inversion*. Springer Science & Business  
238 Media.
- 239 Fichtner, A., Kennett, B. L. N., Igel, H., & Bunge, H. P., 2010. Full waveform tomography for  
240 radially anisotropic structure: new insights into present and past states of the Australasian upper  
241 mantle. *Earth and Planetary Science Letters* 290(3–4), 270–280.
- 242 Fichtner, A., & Trampert, J., 2011. Resolution analysis in full waveform inversion. *Geophysical*  
243 *Journal International* 187(3), 1604–1624.
- 244 Hirose, F., Nakajima, J., & Hasegawa, A., 2008. Three-dimensional seismic velocity structure and

### 3-D Crustal Shear Wave Velocity Model Derived from the Adjoint Waveform Tomography in the Central

- 245 configuration of the Philippine Sea slab in southwestern Japan estimated by double-difference  
246 tomography. *Geophysical Research: Solid Earth* 113(B9).
- 247 Kato, A., & Nakagawa, S., 2020. Detection of deep low-frequency earthquakes in the Nankai sub-  
248 duction zone over 11 years using a matched filter technique. *Earth Planets Space* 72, 128.
- 249 Komatitsch, D., & Tromp, J., 1999. Introduction to the spectral element method for three-dimensional  
250 seismic wave propagation. *Geophysical journal international* 139(3), 806–822.
- 251 Komatitsch, D., & Tromp, J., 2002. Spectral-element simulations of global seismic wave propagation—  
252 i. validation. *Geophysical Journal International* 149(2),390–412.
- 253 Lei, W., Ruan, Y., Bozdağ, E., Peter, D., Lefebvre, M., Komatitsch, D., Tromp, J., Hill, J., Pod-  
254 horszki, N., & Pugmire, D., 2020. Global adjoint tomography model glad-m25. *Geophysical*  
255 *Journal International* 223(1), 1–21.
- 256 Maeda, T., Obara, K., Furumura, T., & Saito, T., 2011. Interference of long-period seismic wave-  
257 field observed by the dense hi-net array in japan. *Journal of Geophysical Research: Solid Earth*  
258 116(B10).
- 259 Maggi, A., Tape, C., Chen, M., Chao, D., & Tromp, J., 2009. An automated time-window selection  
260 algorithm for seismic tomography. *Geophysical Journal Inter-national* 178(1), 257–281.
- 261 Miyoshi, T., Obayashi, M., Peter, D., Tono, Y., & Tsuboi, S., 2017. Adjoint tomography of the crust  
262 and upper mantle structure beneath the kanto region using broadband seismograms. *Progress*  
263 *in Earth and Planetary Science* 4(1), 1–20.
- 264 Mora, P., 1987. Nonlinear two-dimensional elastic inversion of multioffset seismic data. *Geophysics*  
265 52, 1211–1228.
- 266 Nakajima, J., & Hasegawa, A., 2007a. Deep crustal structure along the niigata-kobe tectonic zone,  
267 japan: Its origin and segmentation. *Earth, planets and space* 59(2), e5–e8.
- 268 Nakajima, J., & Hasegawa, A., 2007b. Subduction of the philippine sea plate beneath southwestern  
269 japan: Slab geometry and its relationship to arc magmatism. *Journal of Geophysical Research:*  
270 *Solid Earth* 112(B8).
- 271 Nakajima, J., Hirose, F., & Hasegawa, A., 2009. Seismotectonics beneath the tokyo metropoli-  
272 tan area, japan: Effect of slab-slab contact and overlap on seismicity. *Journal of Geophysical*  
273 *Research: Solid Earth* 114(B8).
- 274 Nakajima, J., & Hasegawa, A., 2016. Tremor activity inhibited by well-drained conditions above a  
275 megathrust. *Nat Commun* 7(1), 13863.
- 276 Nimiya, H., Ikeda, T., & Tsuji, T., 2020. Three-dimensional s wave velocity structure of central  
277 japan estimated by surface-wave tomography using ambient noise. *Journal of Geophysical Re-*  
278 *search: Solid Earth* 125(4), e2019JB019043.
- 279 Nishida, K., Kawakatsu, H., & Obara, K., 2008. Three-dimensional crustal s wave velocity structure

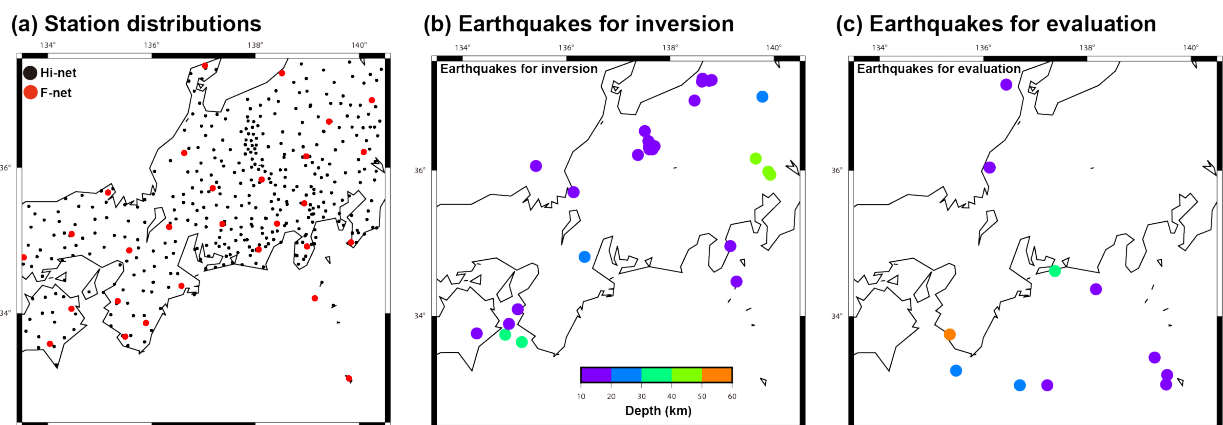
- 280 in japan using microseismic data recorded by hi-net tiltmeters. *Journal of Geophysical Research:*  
281 *Solid Earth* 113(B10).
- 282 Okada, Y., Kasahara, K., Hori, S., Obara, K., Sekiguchi, S., Fujiwara, H., & Yamamoto, A., 2004.  
283 Recent progress of seismic observation networks in japan-hi-net, f-net, k-net and kik-net-. *Earth,*  
284 *Planets and Space* 56(8), xv–xxviii.
- 285 Peter, D., Komatitsch, D., Luo, Y., Martin, R., Goff, N. L., Casarotti, E., Loher, P. L., Magnoni,  
286 F., Liu, Q., Blitz, C., Nissen-Meyer, T., Basini, P., & Tromp, J., 2011. Forward and adjoint  
287 simulations of seismic wave propagation on fully unstructured hexahedral meshes. *Geophysical*  
288 *Journal International* 186(2), 721–739.
- 289 Seno, T., & Yamasaki, T., 2003. Low-frequency tremors, intraslab and interplate earthquakes in  
290 southwest Japan: From a view point of slab dehydration. *Geophys. Res. Lett* 30, 2171.
- 291 Simutè, S., Steptoe, H., Cobden, L., Gokhberg, A., & Fichtner, A., 2016. Full-waveform inversion  
292 of the japanese islands region. *Journal of Geophysical Research: Solid Earth* 121(5),3722-3741.
- 293 Takano, O., 2002. Changes in depositional systems and sequences in response to basin evolution in  
294 a rifted and inverted basin: an example from the neogeneniigata-shin’etsu basin, northern fossa  
295 magna, central japan. *Sedimentary Geology* 152(1-2), 79–97.
- 296 Tarantola, A., 1984. Inversion of seismic reflection data in the acoustic approximation. *Geophysics*  
297 49, 1259–1266.
- 298 Tape, C., Liu, Q., Maggi, A., & Tromp, J., 2010. Seismic tomography of the southern california  
299 crust based on spectral-element and adjoint methods. *Geophysical Journal International* 180(1),  
300 433–462.
- 301 Tromp, J., Tape, C., & Liu, Q., 2005. Seismic tomography, adjoint methods, time reversal and  
302 banana-doughnut kernels. *Geophysical Journal International* 160.1, 195-216.
- 303 Ueno, H., Hatakeyama, S., Aketagawa, T., Funasaki, J., & Hamada, N., 2002. Improvement of  
304 hypocenter determination procedures in the japan meteorological agency (in japanese). *Q. J.*  
305 *Seismol* 65, 123–134.
- 306 Wessel, P., Smith, W., Scharroo, R., Luis, J., & Wobbe, F., 2013. Generic mapping tools: improved  
307 version released. *Eos, Transactions American Geophysical Union* 94(45), 409–410.
- 308 Yano, T. E., Takeda, T., Matsubara, M., & Shiomi, K., 2017. Japan unified high-resolution relocated  
309 catalog for earthquakes (juice): crustal seismicity beneath the Japanese Islands. *Tectonophysics*  
310 702, 19–28.



311

Figure 1: Map of study area. Black lines and pink area indicate major tectonic lines of Itoigawa-Shizuoka tectonic line (ISTL), Median tectonic line (MTL), and Niigata-Kobe tectonic line (NKTL). Red triangle indicate locations of active volcanoes.

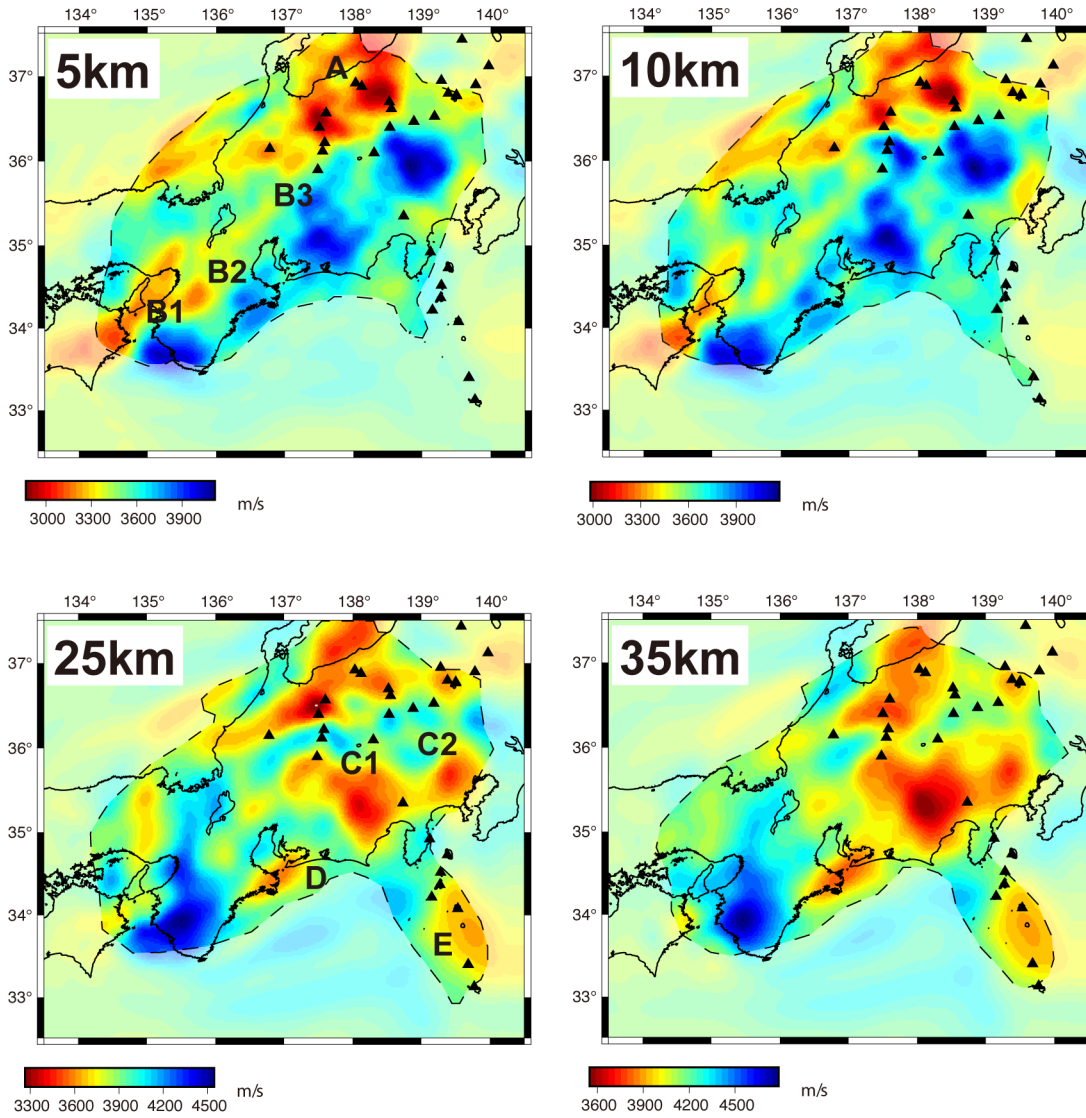
312



313

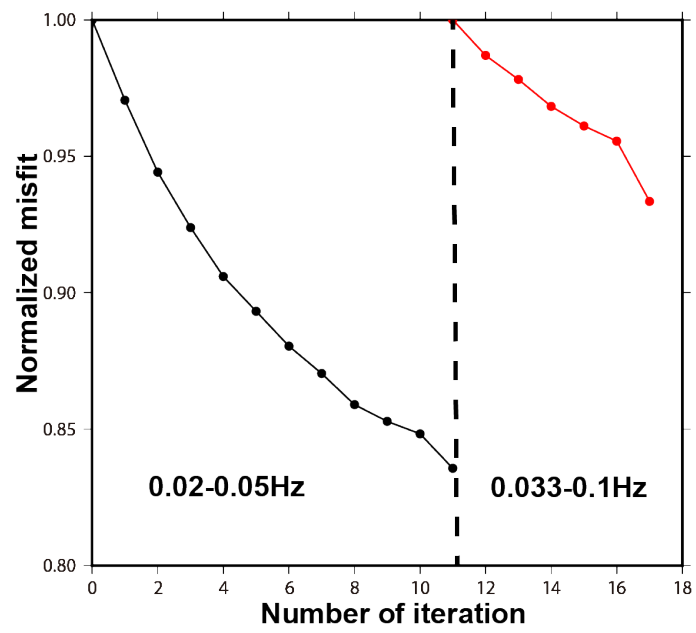
Figure 2: Data. (a)The distributions of Hi-net and F-net stations. (b)Epicenters of earthquakes for inversion. (c)Epicenters of earthquakes for validation.

314



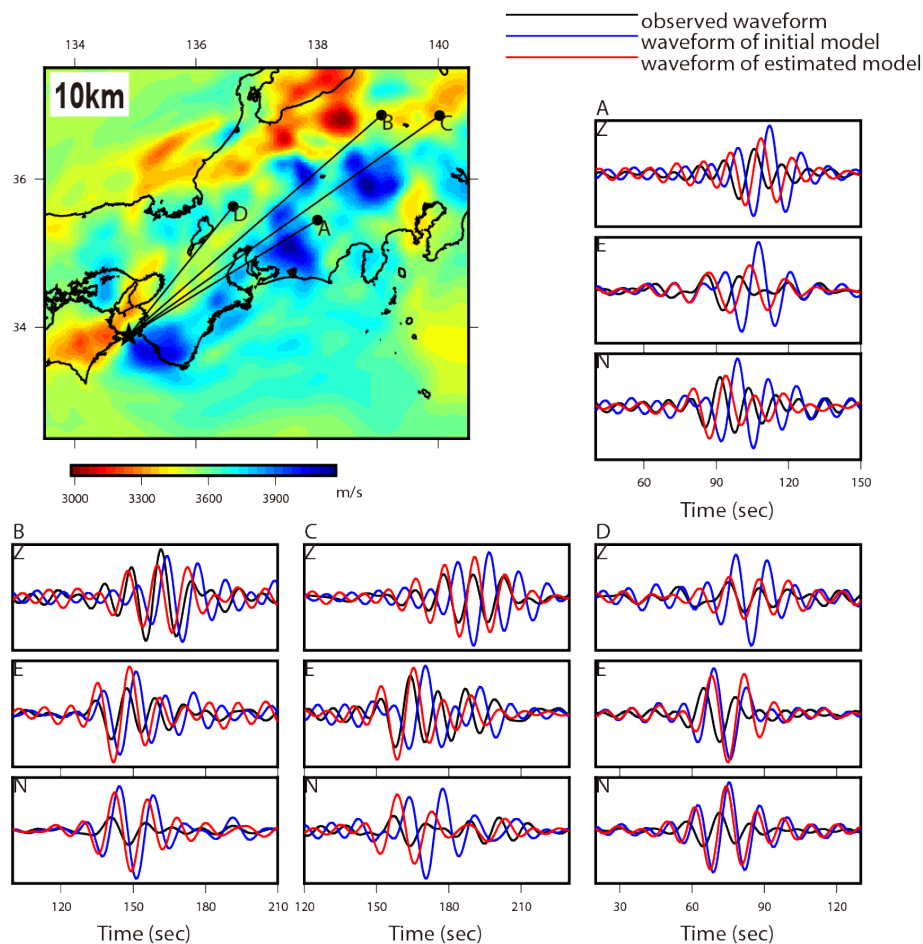
315

Figure 3: Resultant S-wave Velocity model sliced at depths of 5, 10, 25 and 35 *km*. The region enclosed by black dashed line is interpretable area explained in section 5. Black triangles show the locations of active volcanoes.



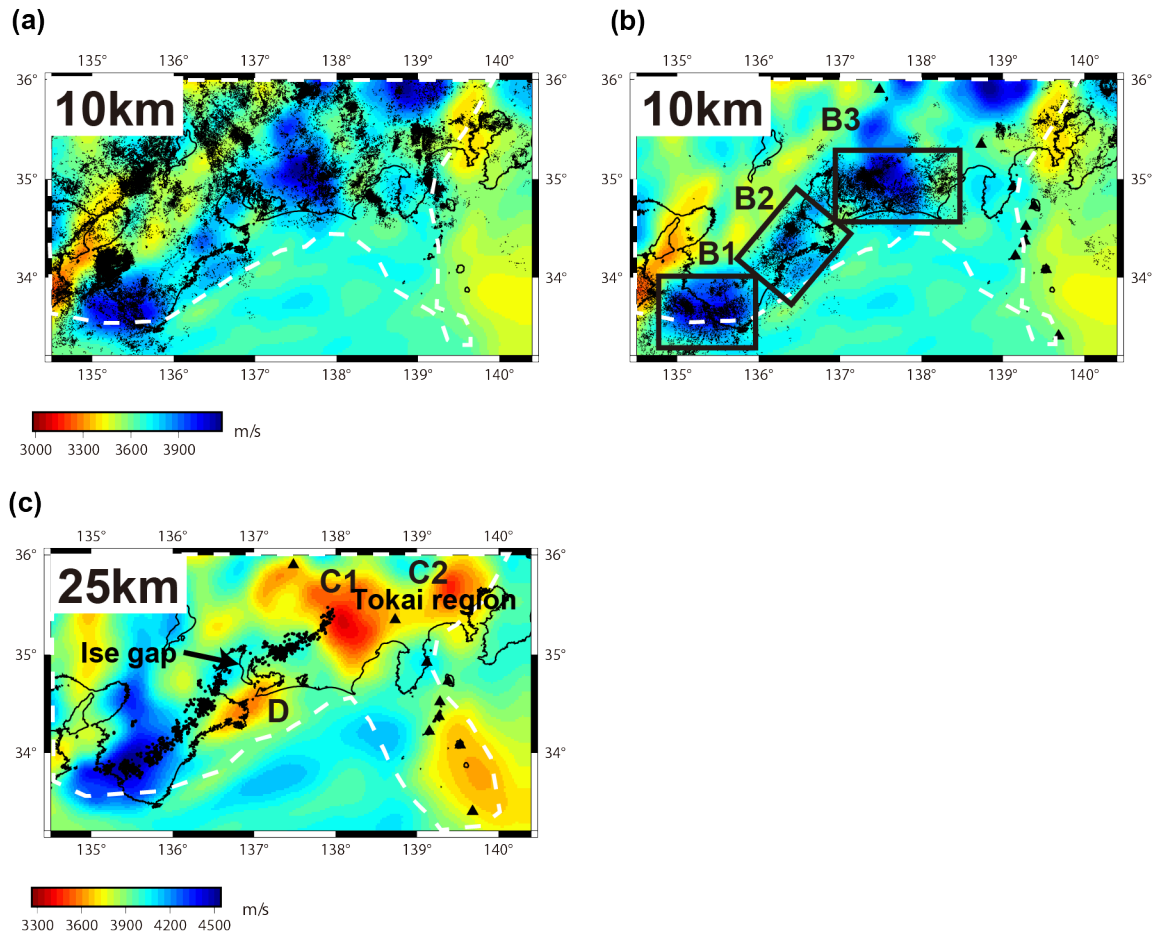
316

Figure 4: Misfit reduction. Normalized misfit reductions in the frequency ranges 0.02–0.05 and 0.033–0.1 Hz, respectively.



317

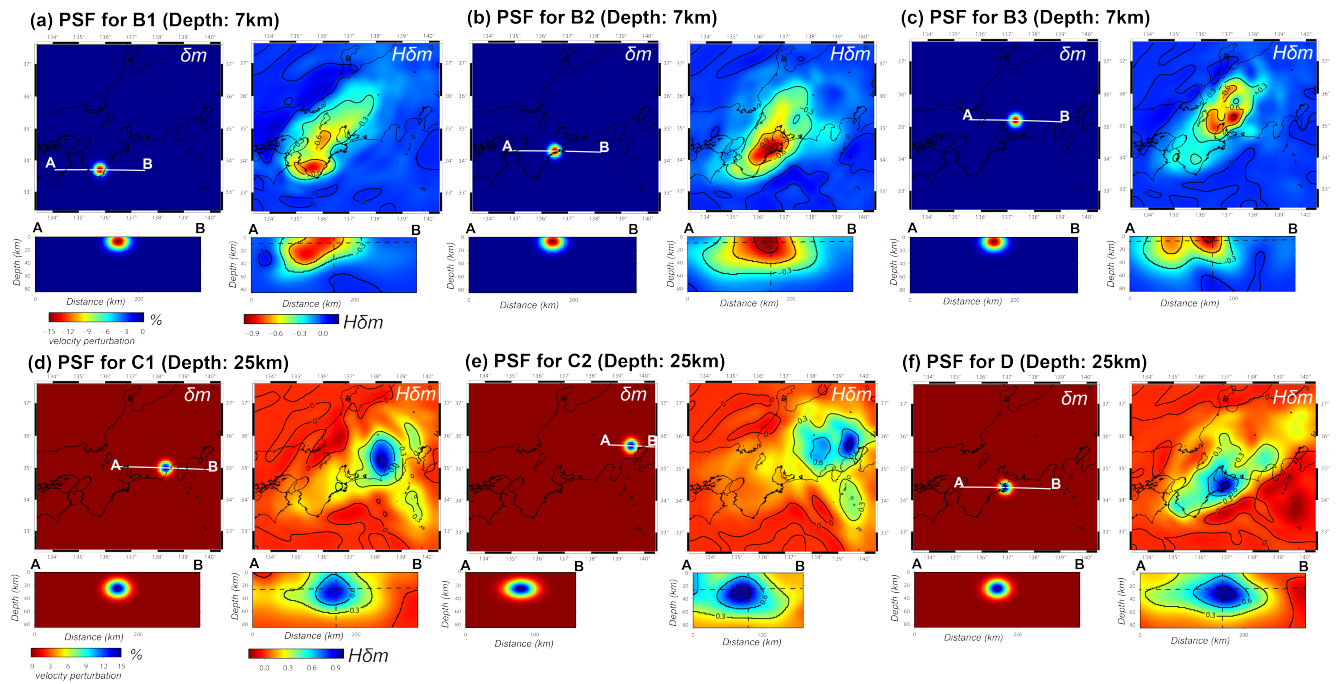
Figure 5: The improvement of waveform fittings. The upper-left subfigure shows S-wave velocity model at 10 km depth. The black star and circles indicate the epicenters and seismometers, respectively. Panels A–D show observed waveforms (black lines), waveforms of the initial model (blue lines), and waveforms of the final model (red lines), corresponding to the seismometers in the top-left figure. In each panel, vertical (Z), eastward (E), and northward (N) components are shown.



318

Figure 6: Zoom of S-wave velocity model. (a) S-wave velocity at 10 km depth with distributions of epicenters at depth < 25 km. (b) S-wave velocity at 10 km depth with distributions of epicenters at depth between 25 and 50 km. (c) S-wave velocity at 20 km depth with distributions of low-frequency earthquakes. White dashed lines are same as black dashed lines in figures 3. The distributions of epicenters of panel(a) and (b) were taken from Yano et al. (2017). The locations of low-frequency earthquakes were estimated by Kato et al. (2020).

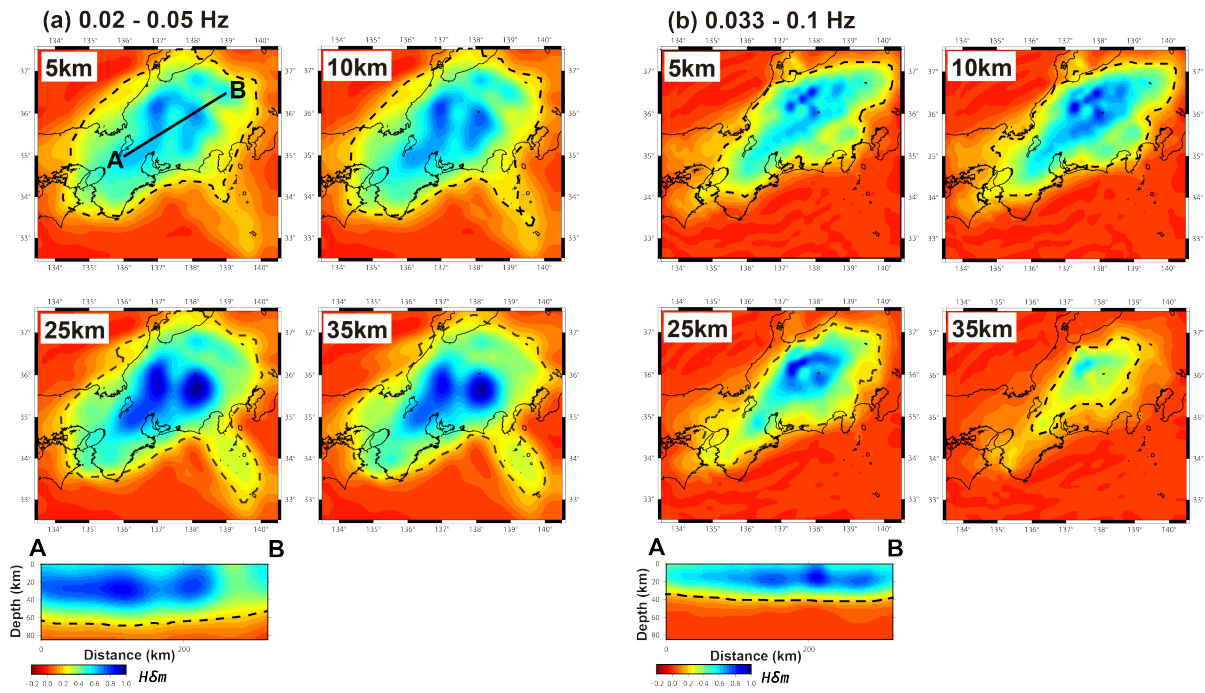
319



320

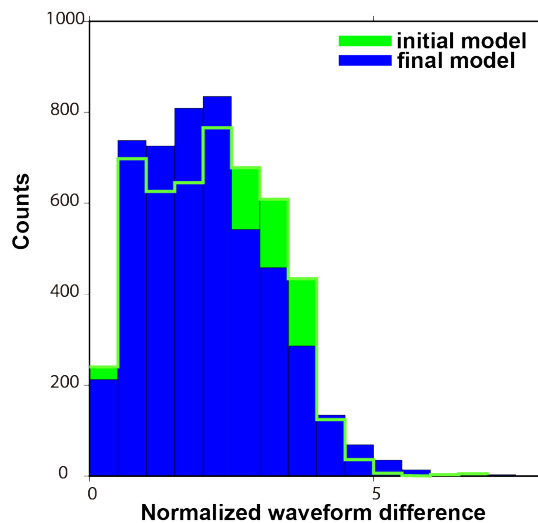
Figure 7: Results of PSFs test using 3D Gaussian functions. At each panel, upper two figures are horizontal sliced images and below two figures are vertical section of white line AB shown in upper left subfigure. The perturbations from final model are shown in percentage for  $\delta m$  and the responses  $H\delta m$  are normalized.

### 3-D Crustal Shear Wave Velocity Model Derived from the Adjoint Waveform Tomography in the Central



321

Figure 8: Results of PSFs test using constant volumetric velocity perturbation. (a) Normalized  $H\delta m$  for lower frequency range 0.02-0.05 Hz. Horizontal sliced  $H\delta m$  are shown in upper 4 subfigures and vertical section of black line AB is shown in bottom subfigure. The values of regions enclosed by black dashed lines are  $> 0.2$ . (b) This panel is same as panel (a), but shows the results for higher frequency range 0.033-0.1 Hz.



322

Figure 9: Normalized waveform difference of initial and final model for validation dataset.